Geminate and Nongeminate Pathways for Triplet Exciton Formation in Organic Solar Cells

Alberto Privitera, Jeannine Grüne, Akchheta Karki, William K. Myers, Vladimir Dyakonov, Thuc-Quyen Nguyen, Moritz K. Riede, Richard H. Friend, Andreas Sperlich,* and Alexander J. Gillett*

Organic solar cells (OSCs) have recently shown a rapid improvement in their performance, bringing power conversion efficiencies to above 18%. However, the open-circuit voltage of OSCs remains low relative to their optical gap and this currently limits efficiency. Recombination to spin-triplet excitons is a key contributing factor, and is widely, but not universally, observed in donor–acceptor blends using both fullerene and nonfullerenes as electron acceptors. Here, an experimental framework that combines time-resolved optical and magnetic resonance spectroscopies to detect triplet excitons and identify their formation mechanisms, is reported. The methodology is applied to two well-studied polymer:fullerene systems, PM6:PC$_{60}$BM and PTB7-Th:PC$_{60}$BM. In contrast to the more efficient nonfullerene acceptor systems that show only triplet states formed via nongeminate recombination, the fullerene systems also show significant triplet formation via geminate processes. This requires that geminate electron–hole pairs be trapped long enough to allow intersystem crossing. It is proposed that this is a general feature of fullerene acceptor systems, where isolated fullerenes are known to intercalate within the alkyl sidechains of the donor polymers. Thus, the study demonstrates that engineering good donor and acceptor domain purity is key for suppressing losses via triplet excitons in OSCs.

1. Introduction

Driven by the recent development of nonfullerene electron acceptor (NFA) materials, the power conversion efficiencies (PCEs) of organic solar cells (OSCs) have rapidly increased, and now exceed 18%.[1–5] However, the photon energy loss in OSCs, defined as the difference between the optical gap (E_g) and the energy of the extracted charges (qV_{OC}),[6] where q is the elementary charge and V_{OC} is the open-circuit voltage, remains high and is now the main factor limiting OSC performance.[7,8] The primary cause is excessive nonradiative recombination in OSCs,[9] which impacts the V_{OC} of the solar cell by reducing the charge carrier lifetime from the intrinsic radiative limit.[10–12] This non radiative voltage loss (ΔV_{nr}) can be directly calculated from the electroluminescence external quantum efficiency (EQE$_{EL}$) of the solar cell run at moderate forward bias as a light-emitting diode

$$\Delta V_{nr} = \frac{-k_B T}{q} \ln\left(EQE_{EL}\right) \tag{1}$$

where k_B is the Boltzmann constant and T is temperature. Here, the EQE$_{EL}$ can be further separated into the different contributions[13]

$$EQE_{EL} = \gamma \Phi_{PL} \chi \eta_{out} \tag{2}$$

where γ is the charge balance factor, Φ_{PL} is the photoluminescence quantum efficiency, χ is the fraction of recombination

A. Privitera, M. K. Riede
Clarendon Laboratory
University of Oxford
Parks Road, Oxford OX1 3PU, UK
A. Privitera
Department of Chemistry
University of Torino
Via Giuria, Torino, Torino 10125, Italy
J. Grüne, V. Dyakonov, A. Sperlich
Experimental Physics 6
Julius Maximilian University of Würzburg
Am Hubland, Würzburg 97074, Würzburg, Germany
E-mail: sperlich@physik.uni-wuerzburg.de

The ORCID identification number(s) for the author(s) of this article can be found under https://doi.org/10.1002/aenm.202103944.

A. Karki, T.-Q. Nguyen
Centre for Polymers and Organic Solids
Department of Chemistry and Biochemistry
University of California at Santa Barbara
Santa Barbara, CA 93106, USA
W. K. Myers
Centre for Advanced ESR
Inorganic Chemistry Laboratory
University of Oxford
South Parks Road, Oxford OX1 3QR, UK
R. H. Friend, A. J. Gillett
Cavendish Laboratory
University of Cambridge
JJ Thomson Avenue, Cambridge CB3 0HE, UK
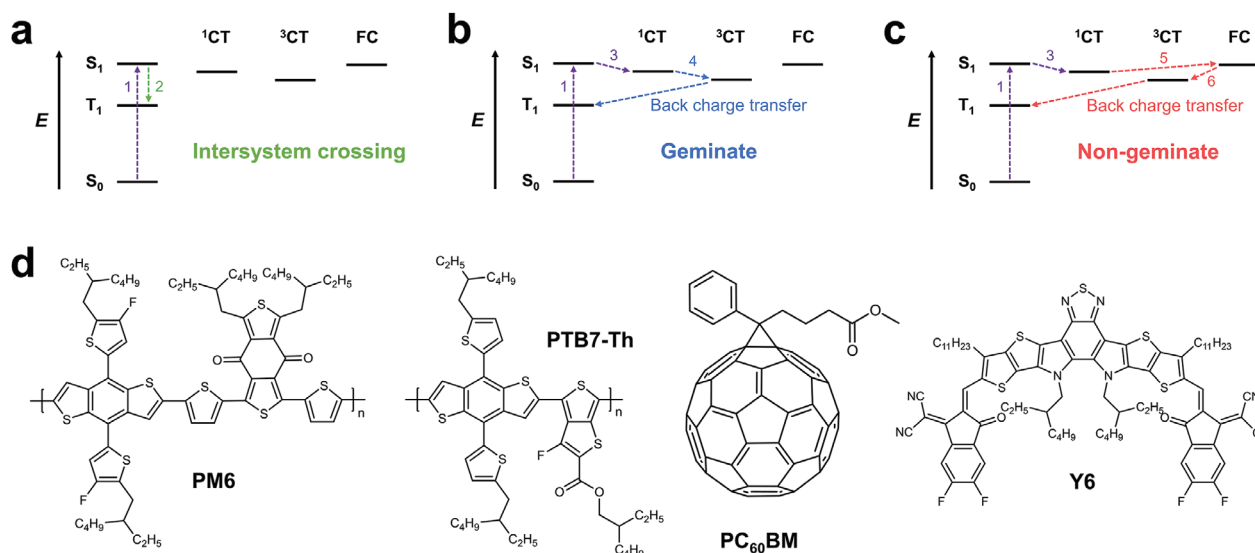E-mail: ajg216@cam.ac.uk

Figure 1. Triplet formation pathways and organic solar cell materials studied. a) Schematic of the direct intersystem crossing pathway for T_1 formation in organic solar cells. 1) After optical excitation into S_1, charge transfer to the ^1CT state does not occur and 2) T_1 is formed by intersystem crossing instead. b) Schematic of the geminate BCT pathway for T_1 formation in organic solar cells. 1) After optical excitation into S_1, 3) charge transfer to the ^1CT state successfully occurs. 4) However, the ^1CT state does not separate into free charges (FC) and instead undergoes spin-mixing to form ^3CT states. These ^3CT states then undergo a spin-allowed back charge transfer process to form molecular T_1 states. c) Schematic of the nongeminate BCT pathway for T_1 formation in organic solar cells. 1) After optical excitation into S_1, 3) charge transfer to the ^1CT state successfully occurs. 5) ^1CT then separates into free charges. 6) Spin-statistical nongeminate recombination of free charges leads to the formation of ^3CT states, which can then undergo back charge transfer to form molecular T_1 states. d) The chemical structures of the two donor polymers and the fullerene acceptor material used in this study. The structure of the nonfullerene acceptor Y6 is included for reference in the discussion of the PLQE results.

events that can decay radiatively (spin-singlet excitations) and η_{out} is the photon out-coupling efficiency. To address the low EQE_{EL} of OSCs, recent studies have focused on improving Φ_{PL} of spin-singlet excitations in the donor:acceptor blend.[7,14–16] However, the optimum optical gap for a single junction solar cell lies in the near-infrared spectral region[10,17] where most OSCs show stronger multi-phonon nonradiative recombination rates, termed the energy gap law.[9,18] As such, this may limit the scope for increasing Φ_{PL} of spin-singlet states in such systems.[19]

Recently, the recombination of charge carriers via spin-triplet excitons has been identified as another significant nonradiative voltage loss pathway in both fullerene and NFA OSCs.[20–23] For example, in the benchmark PM6:Y6 system,[24] the fraction of charge carriers that recombine via the triplet exciton (T_1) of the low E_g component, Y6, is ≈90%;[20] comparable T_1 recombination fractions have also been reported in fullerene acceptor OSCs.[25,26] As a result, χ in Equation 2 is limited to 0.1 and the EQE_{EL} of the PM6:Y6 blend is reduced by a factor of 10, lowering the V_{OC} by ≈60 mV. We note that to achieve a V_{OC} gain comparable to eliminating recombination via T_1, Φ_{PL} of the low E_g component, which is considered to provide the limit for Φ_{PL} of the blend when recombination can proceed via the lowest energy singlet exciton (S_1),[7,15] should be raised by a factor of 10. To explore the feasibility of such an improvement in luminescence efficiency, we have measured Φ_{PL} for a neat film of the widely used NFA Y6. Here, we obtain $\Phi_{PL} = 2\%$, which would necessitate an increase in Φ_{PL} to ≈20%. A Φ_{PL} of this magnitude would be unprecedented among fluorescent organic small molecules with an emission peak around 950 nm,[19] moreover in a molecule that can also operate as an electron acceptor in a highly efficient OSC. Thus, while enhancing Φ_{PL} can provide incremental

improvements in device performance, it is unlikely to alone yield the step-change in V_{OC} required for PCEs of >20% to be realized in single junction OSCs. Furthermore, triplet states have also been implicated in the degradation of both fullerene and NFA OSC blends, potentially presenting a fundamental barrier to commercial applications which require photovoltaic modules with long term stability.[27–30] Therefore, eliminating recombination via T_1 should now be a key focus for further improving the V_{OC} and operational lifetimes of OSCs. However, we note this remains an understudied topic in the field.[23,31–33] This is likely due to the difficulty in detecting and characterizing spin-triplet states in organic semiconductors, as they are generally optically dark and, in the context of OSCs, often short lived due to the presence of rapid annihilation processes.[20]

2. Probing Recombination via Spin-Triplet Excitons in Organic Solar Cells

We present here an experimental framework for probing triplet excitons in OSCs to assist with the task of engineering out recombination via T_1. We consider that there are three main ways in which T_1 can be created in OSCs: 1) direct intersystem crossing (ISC) from un-dissociated S_1 states (**Figure 1**a); 2) back charge transfer (BCT) from geminate spin-triplet charge transfer (^3CT) states (Figure 1b); 3) BCT from ^3CT states formed via nongeminate recombination (Figure 1c). In general, any T_1 states formed will ultimately relax to the lowest energy T_1 in the system. But, if molecular T_1 states are energetically higher than the ^3CT states, T_1 will not be formed.[34,35] As ^3CT states are readily converted to spin-singlet CT states (^1CT) through the hyperfine interaction

**ADVANCED
SCIENCE NEWS**

www.advancedsciencenews.com

**ADVANCED
ENERGY
MATERIALS**

www.advenergymat.de

(HFI),[36] their presence is not expected to significantly impact device performance.[20] Therefore, T_1 states become a problem if they are energetically below the CT states. However, as the offset between CT states and the lowest energy S_1 is typically small (<0.2 eV) to reduce energy losses associated with charge generation,[7,9,14] the molecular T_1 states almost always lie below the CT states due to the large S_1-T_1 energy gap in most organic semiconductors with localized molecular excitons.[37–39] Furthermore, as most OSC blends comprise at least one donor and one acceptor component, with ternary systems containing an additional donor or acceptor,[2–5,40,41] there is the potential for T_1 states to be formed on any of these materials through each of the three pathways presented above. Thus, fully understanding these complex and overlapping mechanisms will require the application of multiple experimental techniques, each targeting a specific subset of the possible T_1 formation pathways.

To achieve this, we propose the combination of optical and magnetic resonance spectroscopies, which have previously been utilized for investigating T_1 states in organic semiconductors.[20,25,42–45] Specifically, we present a framework to investigate recombination via T_1 through three complementary methods: transient absorption (TA), time-resolved electron paramagnetic resonance (trEPR), and photoluminescence detected magnetic resonance (PLDMR) spectroscopies. In Table S1 in the Supporting Information, we present a summary of the three different techniques, as well as the T_1 recombination pathways that they can detect; a more detailed discussion on each of these techniques is provided with the corresponding experimental results (vide infra) and in the Supporting Information.

To develop our experimental framework, we have chosen to examine two model fullerene OSC systems: PM6:PC$_{60}$BM and PTB7-Th:PC$_{60}$BM (chemical structures in Figure 1d). These blends give PCEs of 7.4% and 7.5%, respectively; further information is given in Figure S1 in the Supporting Information. The polymers PM6 and PTB7-Th have been chosen as they are commonly used donor materials in efficient fullerene and NFA OSCs.[3,24,40,41,46–49] We have opted to use fullerene acceptors for two key reasons. First, unlike NFAs which exhibit strong spectral features in TA,[20,50,51] the fullerene component does not make any significant contribution to the observed TA spectrum in the visible and near infrared probe regions. Thus, the use of fullerene blends avoids the complex superposition of the polymer and NFA spectral features and dynamics, simplifying the data interpretation. Second, in many NFA blends, the geminate BCT pathway to T_1 states is not observed in trEPR.[20] Conversely, fullerene blends often show geminate BCT T_1 formation.[23,43,52,53] Thus, fullerene acceptor blends are the ideal model systems to demonstrate how it is possible to probe the three main T_1 formation mechanisms, clarifying the strength of our approach and the complementarity of optical and magnetic resonance techniques.

3. Transient Absorption Spectroscopy

3.1. Using Transient Absorption to Detect Triplet States in Organic Solar Cells

We begin by using TA to explore T_1 formation. TA has been widely used to explore the photophysical processes occurring

in OSCs,[20,26,50,51,54,55] as it is able to provide insights into the evolution of both optically bright and dark states on timescales spanning femtoseconds to milliseconds. Thus, TA is well suited to probing optically dark T_1 states in OSCs as the distinct T_1 photoinduced absorption (PIA) signatures, typically located in the near-infrared (NIR) spectral region,[20–22,25,26,56] are a clear fingerprint for the presence and molecular location of these states. Furthermore, TA can, in theory, distinguish between the presence of a monomolecular (direct ISC or geminate BCT) or bimolecular (nongeminate BCT) T_1 formation pathways through the fluence dependence of T_1 generation; monomolecular pathways show no fluence dependence,[56] while bimolecular events exhibit a strong fluence dependence.[20,25,26] However, in the case where significant bimolecular pathways are present, the fluence dependent behavior of T_1 formation will dominate, masking any underlying monomolecular processes. Thus, as many fullerene and NFA OSCs blends demonstrate nongeminate BCT T_1 formation,[20–22,25,26] TA can, in general, only be reliably used to detect the nongeminate pathway.

3.2. Transient Absorption of PM6:PC$_{60}$BM

In **Figure 2**a, we present the TA from the NIR region of PM6:PC$_{60}$BM. At 0.2–0.3 ps after photoexcitation at 600 nm, we observe the presence of a PIA centered around 1175 nm. Through comparison to the TA of a neat PM6 film (Figure S2, Supporting Information), we attribute this feature to the S_1 state of PM6. The PM6 S_1 is rapidly quenched within a picosecond, indicating ultrafast electron transfer to PC$_{60}$BM. Subsequently, over timescales of hundreds of picoseconds, we notice the formation of a new PIA band peaking at the edge of our probe range around 1650 nm. As the T_1 PIA for PC$_{60}$BM has previously been reported at 720 nm,[57,58] we attribute this new PIA to T_1 located on PM6. We also observe a strong fluence dependence for the formation of this new PIA (Figure 2b), indicating that the nongeminate BCT process plays a large part in PM6 T_1 formation. In the highest fluence measurement for PM6:PC$_{60}$BM presented here (6 μJ cm^{-2}), we note that the rise in the T_1 PIA begins to flatten out towards 2 ns; this can be attributed to the competing effects of triplet-charge annihilation (TCA). As the rate of TCA depends on the charge carrier density in the blend film (as well as the charge carrier mobility[25]), it is expected to become more prominent on subnanosecond timescales under higher excitation fluences.[20,25,26] Indeed, TCA is the primary nonradiative quenching pathway of T_1 in OSCs and is therefore directly responsible for the increased nonradiative voltage losses in OSCs with significant T_1 formation.[20,23,38]

3.3. Transient Absorption of PTB7-Th:PC$_{60}$BM

We next discuss the TA from the NIR region of the PTB7-Th:PC$_{60}$BM blend (Figure 2c). At 0.1–0.15 ps after photoexcitation at 700 nm, we observe two PIA features: one peaked at 1125 nm and a broader band extending towards the edge of our probe range at 1450 nm. The PIA at 1125 nm is attributed to
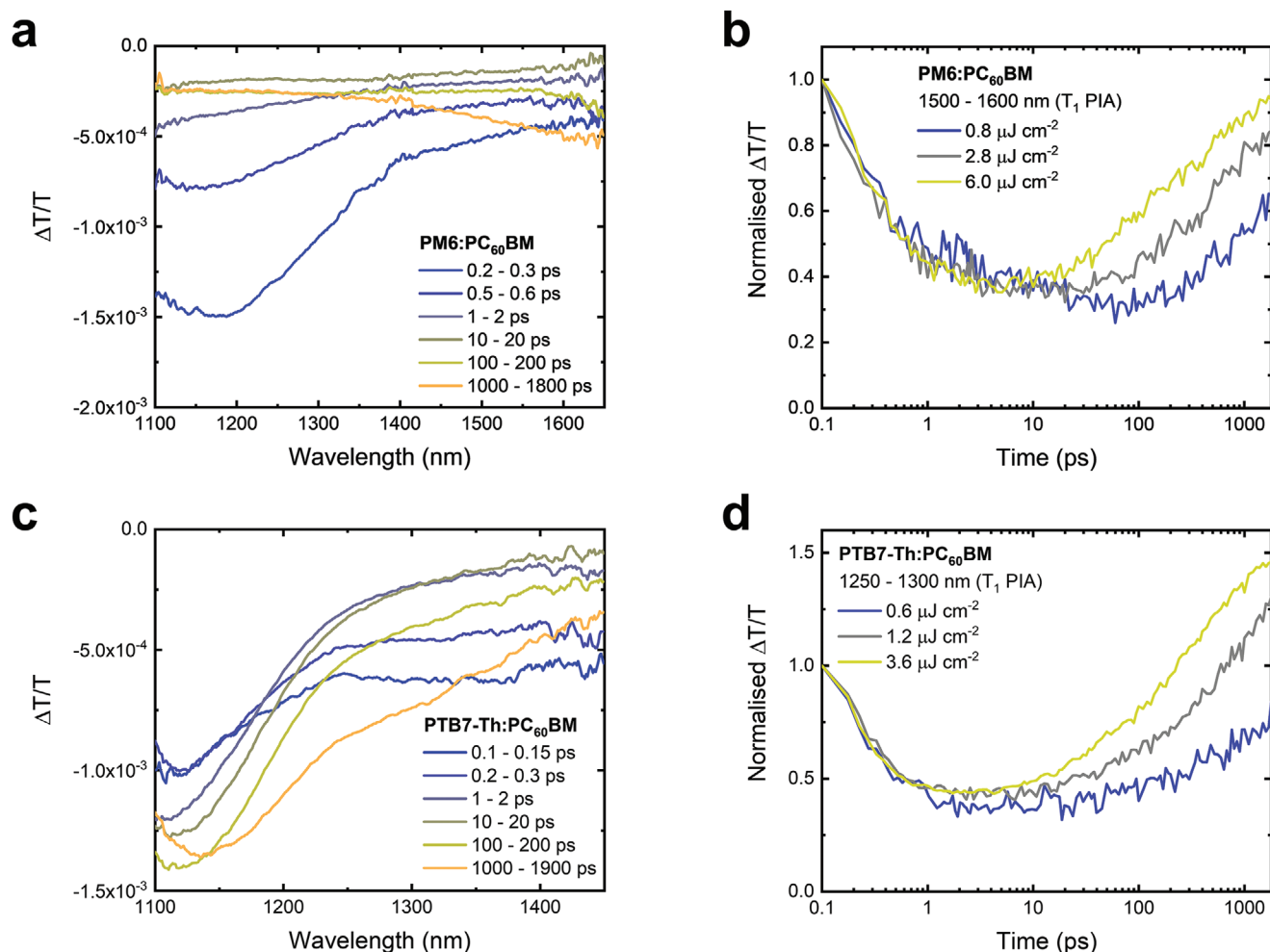
**ADVANCED
SCIENCE NEWS**

www.advancedsciencenews.com

**ADVANCED
ENERGY
MATERIALS**

www.advenergymat.de

Figure 2. Transient absorption spectroscopy of the organic solar cell blends studied. a) The TA spectra of a PM6:PC$_{60}$BM blend film, excited at 600 nm with a fluence of 2.8 μJ cm^{-2}. The PM6 S$_1$ PIA centred at 1175 nm decays within the first picosecond due to electron transfer to PC$_{60}$BM. Over hundreds of picoseconds, a new PIA band around 1650 nm begins to grow in, indicating recombination into PM6 T$_1$ states. b) The TA kinetics a PM6:PC$_{60}$BM blend film, excited at 600 nm with varying fluence. The fluence dependence of the T$_1$ PIA growth shows that T$_1$ formation occurs following the bimolecular recombination of free charge carriers. c) The TA spectra of a PTB7-Th:PC$_{60}$BM blend film, excited at 700 nm with a fluence of 3.6 μJ cm^{-2}. The PTB7-Th S$_1$ PIA band around 1400 nm decays within the first picosecond due to electron transfer to PC$_{60}$BM, leaving behind the PTB7-Th hole polaron PIA at 1125 nm. Over hundreds of picoseconds, a new PIA band on the low energy edge of the hole polaron around 1300 nm begins to grow in, indicating recombination into PTB7-Th T$_1$ states. d) The TA kinetics a PTB7-Th:PC$_{60}$BM blend film, excited at 700 nm with varying fluence. The fluence dependence of the T$_1$ PIA region growth shows that T$_1$ formation occurs following the bimolecular recombination of free charge carriers. All TA measurements were performed at 293 K.

the hole polaron located on PTB7-Th,[59] while the band around 1450 nm is confirmed to be the residual PTB7-Th S$_1$ PIA though comparison with the TA spectrum of a neat PTB7-Th film (Figure S3, Supporting Information). As with PM6:PC$_{60}$BM, the rapid quenching of the S$_1$ PIA indicates ultrafast electron transfer from the electron donor polymer to the fullerene. However, unlike PM6:PC$_{60}$BM, we do not observe the formation of a clear T$_1$ PIA over timescales of hundreds of picoseconds. Rather, we see an apparent broadening on the low energy edge of the hole polaron PIA. Kinetic traces from this region around 1250–1300 nm reveal a clear fluence dependence (Figure 2d), indicating a bimolecular formation mechanism. Thus, in-line with a previous report,[59] we conclude that the PIA of PTB7-Th T$_1$ states, formed via the nongeminate BCT process, overlaps with the hole PIA.

4. Time-Resolved Electron Paramagnetic Resonance Spectroscopy

4.1. Using trEPR Spectroscopy to Detect Triplet States in Organic Solar Cells

Having explored the nongeminate BCT pathway, we now investigate the geminate BCT and direct ISC pathways for T$_1$ formation using trEPR spectroscopy. trEPR typically has a time resolution on the order of hundreds of nanoseconds and is sensitive to the presence of states with unpaired spins;[60,61] in OSCs, this primarily includes T$_1$ states, spin-correlated radical pairs (which can be considered analogous to CT states in an OSC blend), and free charge carriers.[43,52,53] With a focus on T$_1$ states, trEPR not only provides information on the molecular

location of T_1 and the local structure in the blend through the zero-field splitting (ZFS) parameters of the spin Hamiltonian, but also on the T_1 formation mechanism through the spin-polarization of the signal.[60,62] In trEPR spectroscopy, the spin-polarization results from non-Boltzmann population of the triplet sublevels, which manifests as a characteristic polarization pattern of absorptive (*a*) and emissive (*e*) microwave-induced EPR transitions between the three triplet sublevels. For example, direct ISC mediated by spin-orbit coupling (SOC) from S_1 results in a spin selective population of the zero-field triplet sublevels (Table S2, Supporting Information),[63] which in turn is converted into a polarized population of the three high-field triplet sublevels T_+, T_0, and T_-. By applying microwave irradiation, transitions between these sublevels result in an *aaaeee*, *eeeaaa*, *eeaeaa*, *aaeaee*, *aeaeae* or *eaeaea* polarization pattern. In contrast, T_1 created through the geminate BCT mechanism will possess a characteristic *aeeaae* or *eaaeea* signature. This is because ISC in the CT state manifold, which is primarily mediated by the HFI with paramagnetic nuclei (mainly protons), results in an overpopulation of the T_0 sublevel of the ^3CT state and thus also the molecular T_1 state following BCT.[27,53] In contrast, nongeminate recombination does not produce spin polarization as the spin-statistical recombination of uncorrelated free charge carriers to T_1 via ^3CT results in an equal population of the T_+, T_0, and T_- sublevels. The equal sublevel population will establish Boltzmann population within the spin-lattice relaxation time, but in the low-field (≈ 330 mT) regime that we explore here with X-band EPR, the spin polarization is too low to be detected with trEPR.[62] Therefore, the nongeminate BCT pathway does not induce a sufficiently high spin-polarization in T_1, and states populated through this mechanism are not observed in trEPR. Thus, trEPR provides an excellent complement to TA spectroscopy, in which only the nongeminate pathway can be reliably detected.

4.2. trEPR of PM6:PC$_{60}$BM

In **Figure 3**a,b, we show the trEPR spectra and associated simulations of the PM6:PC$_{60}$BM film taken at two representative time points (1 and 5 µs) after excitation at 532 nm. A summary of the best fit simulation parameters for the blends studied is included in **Table 1**, with more detailed information on all samples in Table S2 in the Supporting Information. At 1 µs, we observe an intense and spectrally narrow *aeae* feature centered at ≈ 346 mT, assigned to CT states; by 5 µs, this evolves into a pure *a* signal, indicative of free charges (polarons).[61] Conversely, the broader signal between 290 and 410 mT is assigned to T_1 states. From the best-fit spectral simulation at 1 µs, an *eeeaaa* polarization pattern is obtained, confirming that the T_1 states are formed via SOC-ISC; this results from photogenerated S_1 states that do not undergo charge transfer at the donor:acceptor interface. The T_1 ZFS parameters, $D = 1300$ MHz and $E = 140$ MHz, are comparable to the those obtained at 1 µs in a neat PM6 film (Figure S4, Supporting Information) and are significantly larger than those found for a neat PC$_{60}$BM film (Figure S5, Supporting Information; $D = -237$ MHz and $E = 39$ MHz).

Therefore, we assign this feature to the T_1 of PM6. By 5 µs, there is a clear evolution of the polarization pattern, and a more complex spectrum is observed. We attempt to simulate this new spectrum using a single SOC-ISC component but find through examining the residual that this species alone is not sufficient to obtain a high-quality fit (Figure S6, Supporting Information). An excellent fit is only obtained when two T_1 species ($D = 1220$ MHz and $E = 40$ MHz) are included in the simulation with distinct *aeaeae* and *eaaeea* polarization patterns. The *aeaeae* species is the same as the PM6 T_1 formed via SOC-ISC at 1 µs, with the apparent spectral inversion attributed to an unequal rate of decay from the three high-field triplet sublevels.[64] However, the new *eaaeea* contribution represents T_1 formed via the geminate BCT mechanism, confirming that this pathway is also present in the PM6:PC$_{60}$BM blend.

4.3. trEPR of PTB7-Th:PC$_{60}$BM

We now turn to the PTB7-Th:PC$_{60}$BM blend film (Figure 3c,d). At both 1 and 5 µs, this blend shows a strong *ea* feature at ≈ 346 mT, which is assigned to CT states.[61] In addition, we also observe a signal between 300 and 390 mT at both 1 and 5 µs; as the spectrum is significantly broader than the PC$_{60}$BM T_1, we attribute this feature to T_1 states on PTB7-Th. We verify this assignment through comparison of the ZFS parameters obtained from simulations of the neat PTB7-Th (Figure S7, Supporting Information) and PTB7-Th:PC$_{60}$BM blend films (Table S1, Supporting Information). The T_1 spectra cannot be well-described by a best-fit simulation with single *aaaeee* SOC-ISC species (Figure S8, Supporting Information), confirming that there is more than one T_1 generation mechanism present. Therefore, we have simulated the T_1 spectra at 1 and 5 µs with two species (see Table S1 in the Supporting Information); one with an *aaaeee* and the other with an *eaaeea* polarization pattern, representing T_1 states formed via SOC-ISC and the geminate BCT mechanism, respectively. Thus, we are able to definitively confirm that geminate BCT T_1 formation is also occurring in the PTB7-Th:PC$_{60}$BM.

4.4. Discussion of the trEPR Results

When comparing the blends, we observe the presence of geminate BCT T_1 and CT states at both 1 and 5 µs in PTB7-Th:PC$_{60}$BM. In contrast, we only see BCT T_1 states at 5 µs in PM6:PC$_{60}$BM and CT states at 1 µs; by 5 µs, the CT states have evolved into free charges in this blend. To better understand these results, we first consider that the time resolution of our trEPR measurements (hundreds of nanoseconds) is too slow to directly monitor the rapid separation of most CT states in an efficient polymer:fullerene blend, which largely takes place on sub-picosecond timescales.[65] Thus, what we observe in trEPR are only the longer lived (trapped) CT states responsible for the geminate BCT T_1 formation mechanism; as discussed above, CT states formed via spin-statistical nongeminate recombination are not detected in trEPR. In OSCs, CT states can be discussed in the context of the spin-correlated radical pair model.[36] Spin-correlated radical pairs are characterised by four eigenstates that in the high field approximation are two mixed singlet-triplet levels with $M_S = 0$, $|^1CT_0\rangle$ and $|^3CT_0\rangle$, and two
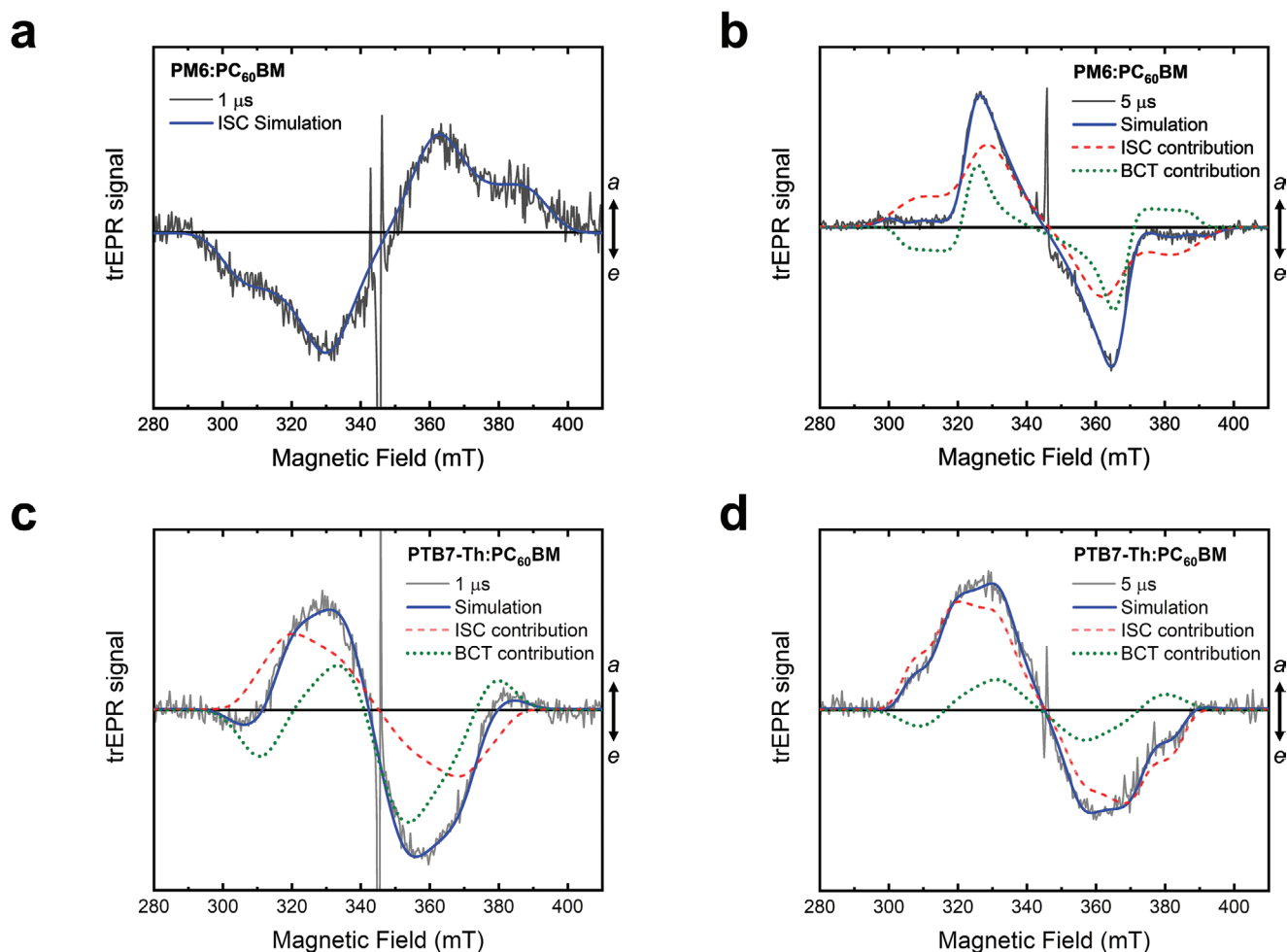
ADVANCED
SCIENCE NEWS
www.advancedsciencenews.com

ADVANCED
ENERGY
MATERIALS
www.advenergymat.de

Figure 3. The trEPR spectra of the organic solar cell blends studied. a) The trEPR spectrum of a PM6:$PC_{60}BM$ blend film at 1 µs, excited at 532 nm. Absorption (*a*) is up, emission (*e*) is down. The central *aeae* species is assigned to a CT state. The PM6 T_1 species can be simulated with a single *eeeaaa* component, indicating it is formed via direct ISC from undissociated S_1 states. b) The trEPR spectrum of a PM6:$PC_{60}BM$ blend film at 5 µs, excited at 532 nm. The *aeae* CT state has now evolved into a single *a* signal, indicative of free charges. The PM6 T_1 species requires the use of two T_1 contributions to successfully describe the observed spectrum. The first is an *aeaeae* component, which is the same ISC T_1 state as the 1 µs spectrum, except inverted. The second is an *eaaeea* component, which is characteristic of T_1 states formed via the geminate BCT mechanism. c) The trEPR spectrum of a PTB7-Th:$PC_{60}BM$ blend film at 1 µs, excited at 532 nm. The central *ea* species is assigned to a CT state. The PTB7-Th T_1 species requires the use of two T_1 contributions to successfully describe the observed spectrum. The first is an *aaaaee* component, indicating T_1 states formed via direct ISC from undissociated S_1 states. The second is an *eaaeea* component, which is characteristic of T_1 states formed via the geminate BCT mechanism. d) The trEPR spectrum of a PTB7-Th:$PC_{60}BM$ blend film at 5 µs, excited at 532 nm. The *ea* CT state is still present, indicating slower generation of free charges in this blend. The PTB7-Th T_1 species requires the use of two T_1 contributions to successfully describe the observed spectrum. The first is an *aaaeee* component, indicating T_1 states formed via direct ISC from undissociated S_1 states. The second is an *eaaeea* component, which is characteristic of T_1 states formed via the geminate BCT mechanism. All trEPR spectra were acquired at 80 K.

Table 1. A summary of the T_1 formation pathways detected by each method in the PM6:$PC_{60}BM$ and PTB7-Th:$PC_{60}BM$ blends. All three blends exhibit the nongeminate BCT, geminate BCT, and SOC-ISC, T_1 formation pathways. TA and trEPR identify T_1 states on the donor (D) polymer, while PLDMR also detects a weak signature of T_1 states on the acceptor (A) fullerene material, likely formed via direct SOC-ISC from undissociated $PC_{60}BM$ S_1 states.

Blend	Nongeminate BCT	Geminate BCT	SOC-ISC	$|D|$, $|E|$ [MHz]	T_1 location
PM6:$PC_{60}BM$	TA	–	trEPR (1 µs)	1300, 140	D
		trEPR (5 µs)	trEPR (5 µs)	1220, 40	
	PLDMR	PLDMR	PLDMR	1500, 70	D, A (weak)
PTB7-Th:$PC_{60}BM$	TA	trEPR (1 µs)	trEPR (1 µs)	1050, 200	D
		trEPR (5 µs)	trEPR (5 µs)	1143, 164	
	PLDMR	PLDMR	PLDMR	1470, 180	D, A (weak)

ADVANCED
SCIENCE NEWS

www.advancedsciencenews.com

ADVANCED
ENERGY
MATERIALS

www.advenergymat.de

pure triplet states with $M_S = \pm 1$, $|^3 CT_+\rangle$ and $|^3 CT_-\rangle$.[53,66] Owing to the energetic splitting due to the Zeeman interaction, mixing can only occur between $|^1 CT_0\rangle$ and $|^3 CT_0\rangle$.[67] The spin-mixing rate in the studied blends is primarily controlled by the HFI and results in a periodic oscillation of the $M_S = 0$ population between $|^1 CT_0\rangle$ and $|^3 CT_0\rangle$ on timescales of tens of nanoseconds.[68] Thus, as the spin mixing timescales are faster than the time resolution of our trEPR measurement, the CT states observed can be considered as an admixture of $|^1 CT_0\rangle$ and $|^3 CT_0\rangle$ in both the PM6:PC$_{60}$BM and PTB7-Th:PC$_{60}$BM blends.

Having clarified this point, we turn to the discussion of our trEPR spectra. To explain why the BCT triplet only appears at 5 µs in PM6:PC$_{60}$BM, we propose that the eventual appearance of free charges in this blend suggests that the CT states are on average more weakly bound than in PTB7-Th:PC$_{60}$BM. This is supported by the PLDMR of the blends (vide infra), where the narrow and negative sign signals arising from free charges (positive and negative polarons) are much more intense in PM6:PC$_{60}$BM (Figure S15, Supporting Information), indicating that a higher proportion of the electrons and holes are far enough apart to no longer be magnetically interacting. A more weakly bound CT state in PM6:PC$_{60}$BM with a larger average electron–hole separation could result in slower BCT for two (related) reasons. First, the BCT rate depends strongly on distance,[20] meaning a ^{3}CT state with greater electron–hole separation would recombine to T$_1$ more slowly. Second, the charges in a more separated ^{3}CT would be expected to approach the donor:acceptor interface, where BCT is fastest, less frequently, also slowing the formation of BCT T$_1$ states. Thus, these two factors can explain the slower appearance of the geminate BCT T$_1$ states in PM6:PC$_{60}$BM.

4.5. Comparison of Fullerene and Nonfullerene Acceptor Systems

We note that the presence of triplet excitons generated by geminate BCT in fullerene acceptor blends, as reported here by us and others,[23,43,52,53] is in clear contrast to the results obtained for the NFA blends.[20] This can be rationalized by the widely observed propensity of fullerene molecules to intercalate within the alkyl side chains of the donor polymer, resulting in the formation of mixed polymer/fullerene regions.[69–73] Of particular relevance to our work, observations of fullerene intercalation within the polymer sidechains have also been made in PC$_{60}$BM blends with polymers from the PTB7 series.[74] We note that efficient solar cell operation is obtained when there is excess fullerene that forms local 5–10 nm fullerene inclusions, driving charge separation from mixed fullerene/sidechain regions to the pure fullerene regions.[72,75–77] However, if the fullerene concentration in these mixed regions falls below the percolation threshold for efficient electron transport, charge separation will be impeded and geminate recombination will result.[75–79] Thus, we propose that poorly-connected fullerene domains provide the opportunity for geminate ^{3}CT formation via HFI-ISC from ^{1}CT states on nanosecond timescales,[56,80] followed by BCT to T$_1$, increasing losses via T$_1$ states. In contrast, many efficient NFA OSCs have been shown to possess good phase purity,[81–84] which has previously been shown to facilitate CT state dissociation and reduce BCT T$_1$ formation.[85] Thus, it appears that

engineering good phase purity in the donor:acceptor bulk heterojunction could be helpful for engineering out BCT T$_1$ generation pathways in OSCs.

5. Photoluminescence-Detected Magnetic Resonance Spectroscopy

5.1. Using PLDMR Spectroscopy to Detect Triplet States in Organic Solar Cells

In contrast to TA and trEPR, PLDMR spectroscopy is generally employed as a steady-state technique when investigating organic semiconductors,[86] though transient iterations with a time resolution on the order of tens of nanoseconds are available.[87] Continuous illumination can also yield spin polarization of the triplet sublevels by unequal recombination rates or triplet accumulation, with subsequent triplet-triplet annihilation processes. Furthermore, while trEPR directly detects reflection changes in the applied microwaves following laser excitation, PLDMR uses optical detection.[30,44,45,86,88] Therefore, the experimental sensitivity is greatly enhanced and PLDMR can detect any triplet excitations that are coupled to the photoluminescence of the sample (for example, via the triplet-triplet annihilation of two molecular T$_1$ which reforms, among other possibilities, one bright S$_1$ state and one dark spin-singlet ground state),[86] not just those that are highly spin polarized. In addition, the enhanced sensitivity of PLDMR allows for "half-field" (HF) signals to be readily resolved; HF transitions represent a first-order forbidden $\Delta m_S = \pm 2$ transition between the T$_+$ and T$_-$ sublevels that is enabled by the strong dipolar interaction between the two localized electron spins of a molecular T$_1$ state.[30,44] These signals provide an additional tool for determining the molecular location of a T$_1$ state, since their magnetic field position depends on the strength of the dipolar interaction.[89] Therefore, HF signals are particularly useful when working with systems where the ZFS parameters of the donor and acceptor T$_1$ states are similar, which is often the case in NFA OSC blends.[20]

In **Figure 4** (enlarged individual spectra are presented in Figures S9–S13 in the Supporting Information), we display the PLDMR spectra of neat films of PC$_{60}$BM (red), PTB7-Th (light green), PM6 (light blue) and the PTB7-Th:PC$_{60}$BM (dark green) and PM6:PC$_{60}$BM (dark blue) blends. A summary of the simulation parameters used for the films is shown in Table 1, with the full spectral simulations and ZFS parameters for each sample provided in Figure S15 and Table S3 in the Supporting Information. The spectra consist of a full-field (FF) region (260–410 mT), corresponding to $\Delta m_S = \pm 1$ transitions, and $\Delta m_S = \pm 2$ HF signals (160–172 mT).

5.2. PLDMR of PC$_{60}$BM

Beginning with neat PC$_{60}$BM (Figure 4, red), we observe a relatively narrow T$_1$ feature in the FF spectrum between 320–350 mT, which can be described with the ZFS parameters $D = 360$ MHz and $E = 50$ MHz. Two additional features (sharp negative signals) are superimposed on the T$_1$ signal at 336.25 mT ($g = 2.0040$) and

ADVANCED
SCIENCE NEWS
www.advancedsciencenews.com

ADVANCED
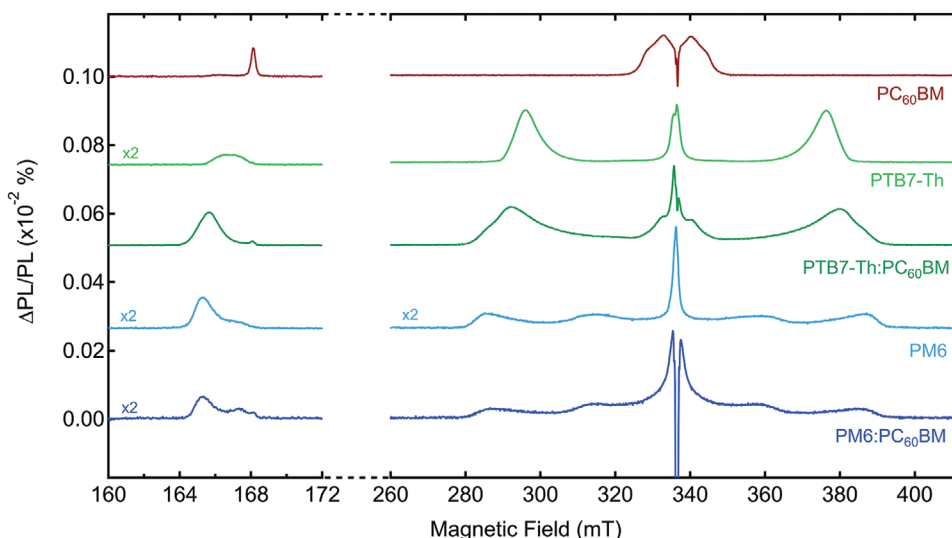ENERGY
MATERIALS
www.advenergymat.de

Figure 4. Photoluminescence-detected magnetic resonance spectra of the neat organic solar cell materials and blends. (Red) The half-field (160–172 mT) and full-field (260–410 mT) PLDMR spectrum of a neat $PC_{60}BM$ film. The HF T_1 signal of $PC_{60}BM$ is visible at 168.1 mT, while the FF T_1 and polaron features are present between 320 and 350 mT. (Light green) The HF and FF PLDMR spectrum of a neat PTB7-Th film. The HF T_1 signal of PTB7-Th is visible at 166.8 mT, while the FF T_1 manifests as the two spectral "wings" 296 and 376 mT. (Dark green) The HF and FF PLDMR spectrum of the PTB7-Th:$PC_{60}BM$ blend film. The HF T_1 signal of PTB7-Th is visible at 165.6 mT, slightly shifted from the neat film due to the changes in the polymer chain ordering upon blending with $PC_{60}BM$. The HF signal of the $PC_{60}BM$ T_1 is weakly visible at 168.1 mT. The FF PTB7-Th T_1 is visible between 280 and 390 mT with a small $PC_{60}BM$ T_1 contribution from 320 to 350 mT. (Light blue) The HF and FF PLDMR spectrum of a neat PM6 film. The HF T_1 signal of PM6 is visible at 165.3 mT, while the FF T_1 is the broad feature spanning 280–390 mT. (Dark blue) The HF and FF PLDMR spectrum of the PM6:$PC_{60}BM$ blend film. The HF T_1 signals of PM6 and $PC_{60}BM$ are visible at 165.3 mT and 168.1 mT, respectively. The FF PM6 T_1 is visible between 280 and 390 mT. All PLDMR spectra were acquired at 10 K.

336.65 mT ($g = 2.0012$), seen more clearly in Figure S9c in the Supporting Information. We assign these to the anion $PC_{60}BM^-$, as already known from literature, and the cation $PC_{60}BM^+$, respectively.[90–92] In addition, a HF signal due to $PC_{60}BM$ T_1 states is also detected at 168.1 mT, which can be easily distinguished from the HF signals of the polymer in the blends.

5.3. PLDMR of PTB7-Th Systems

Neat PTB7-Th (Figure 4, light green) shows a T_1 spectrum with large ordering factor, λ, which provides information on the orientational distribution of the molecules in the sample and is reflected by the outer "wings" in the PLDMR spectra.[62,93,94] In contrast to trEPR, ordering factors are only visible in PLDMR for these materials, further discussed in the Supporting Information. The ordering factor λ is given for θ and ϕ, where θ is the angle between the molecular z-axis and the applied magnetic field, and ϕ is the in-plane angle. If λ is zero, all molecular orientations occur with the same probability. For PTB7-Th, the ordering for θ is $\lambda_\theta = 11$, corresponding to an extremely narrow orientational distribution of the molecules in the direction of the applied magnetic field (Figure S16, Supporting Information). Upon blending PTB7-Th with $PC_{60}BM$ (Figure 4, dark green), a broad T_1 feature of the polymer is clearly visible in the FF and HF signals of the blend. However, the ZFS D-parameter increases from $D = 1190$ MHz in pristine PTB7-Th to $D = 1310$ MHz in the blend, while the ordering factor decreases to $\lambda_\theta = 7.5$. The change in these values suggest that blending PTB7-Th with $PC_{60}BM$ affects the polymer chain

ordering in the PTB7-Th domains, possibly due to fullerene intercalation within the polymer sidechains.[74]

5.4. PLDMR of PM6 Systems

For PM6 (Figure 4, light blue), we observe a broad T_1 spectrum between 280 and 390 mT, corresponding to ZFS parameters $D = 1500$ MHz and $E = 70$ MHz. In contrast to trEPR, this spectrum also shows a considerable ordering factor (Table S3, Supporting Information). When blending PM6 with $PC_{60}BM$ (Figure 4, dark blue), the broader polymer triplet is again clearly visible in the FF and HF signals. In contrast to PTB7-Th:$PC_{60}BM$, the PM6 T_1 ZFS parameters remain the same before and after blending with $PC_{60}BM$ and the ordering factors change only slightly (Table S3, Supporting Information). Thus, the ordering of the polymer chains in PM6 is less disrupted upon mixing with $PC_{60}BM$, when compared to PTB7-Th. Additionally, both blends show a positive ($\Delta PL/PL > 0$) CT state peak with two negative signals at $g = 2.0012$ and $g = 2.0037$ in PTB7-Th:$PC_{60}BM$, and $g = 2.0012$ and $g = 2.0034$ in PM6:$PC_{60}BM$. The lower g value is identical to the negative polaron $PC_{60}BM^-$, as detected in neat $PC_{60}BM$ (Figure S9c, Supporting Information), while the higher g value likely represents positive polarons on the respective polymer.[95]

5.5. Detecting Minority Triplet Formation Pathways with PLDMR

In contrast to trEPR, the additional experimental sensitivity of PLDMR enables us to resolve the weaker $PC_{60}BM$ T_1 signal

in the HF (168.1 mT) regions in both blends (Figures S11a and S13a, Supporting Information) and in the FF (320–350 mT) region of PTB7-Th: $PC_{60}BM$ (Figure S11b, Supporting Information); only the more intense T_1 features of the donor polymers are seen in the corresponding trEPR data (Figure 3). Thus, without PLDMR, minority T_1 generation pathways could easily be missed. When considering the formation mechanism for $PC_{60}BM$ T_1 states in the blends, we note that they are generally too high in energy ($T_1 \approx 1.5$ eV) to be populated by BCT from the CT states in low band gap polymer:fullerene systems with large S_1-CT energetic offsets (as is the case in the blends studied here).[34] Furthermore, as the $PC_{60}BM$ T_1 will be higher in energy than the T_1 states of PM6 and PTB7-Th, assuming a typical S_1-T_1 energy gap of ≈ 0.6–1 eV in most conjugated polymers,[39] any $PC_{60}BM$ T_1 states formed near the donor:acceptor interface would be expected to relax into the lower lying polymer T_1 state. Therefore, we conclude that the $PC_{60}BM$ T_1 states observed must be located in isolated $PC_{60}BM$ domains, which are often found in polymer:fullerene bulk heterojunction blends.[74,76] This observation reinforces the importance of ensuring that domain sizes are on the order of the singlet exciton diffusion length to enable efficient charge generation and suppressed T_1 formation via direct SOC-ISC from undissociated S_1 states.[96]

6. Conclusion

In this work, we have shown that through leveraging the strengths of TA, trEPR, and PLDMR spectroscopies, a complete picture of T_1 generation pathways in OSCs can be obtained. This strategy is fully applicable to both fullerene and NFA blends and will prove valuable in the task of engineering out of recombination via T_1 states in OSCs. Through applying this methodology to two model OSC blends, we have demonstrated that it is possible to unravel the intricacies of spin-triplet physics in OSCs by identifying both the molecular localization and generation mechanism for the wide range of T_1 states found in these systems. Consequently, we have shown that fullerene blends frequently exhibit the geminate BCT T_1 formation mechanism,[23,43,52,53] in addition to the nongeminate pathway. This is in clear contrast to the more efficient NFA OSC systems where the geminate pathway appears to be absent, consistent with their improved performance.[20] We propose that the geminate BCT mechanism is associated with isolated fullerene molecules trapped in alkyl side chains of the donor polymers,[69–73] suggesting that engineering good purity in the donor and acceptor phases is key for suppressing this process. Thus, we anticipate that this framework will also be particularly useful for analyzing T_1 loss mechanisms in ternary systems comprised of both fullerene and NFAs, which have demonstrated some of the highest PCEs to date.[40,41]

7. Experimental Section

OSC Device Fabrication: Indium tin oxide (ITO) patterned glass substrates were cleaned by scrubbing with soapy water, followed by sonication in soapy water, deionized (DI) water, acetone, and isopropanol

for 20 minutes each. The substrates were dried using compressed nitrogen and placed in an oven overnight at 100°C. The conventional architecture devices were made by treating the ITO substrates with UV-ozone for 15 minutes and spin-coating a layer of poly(3,4-ethylenedioxythiophene):poly(styrenesulfonate) (PEDOT:PSS, Clevios P VP Al 8043) at 3000 rpm for 40 s onto the ITO substrates in air. The substrates were then annealed in air at 150 °C for 20 minutes. 1 mg/mL of the cathode interlayer PDINO was dissolved in methanol and spin-coated on top of the active layer. The substrates were then pumped down under vacuum ($<10^{-7}$ torr), and a 100 nm thick Al electrode was deposited on top by thermal evaporation using the Angstrom Engineering Series EQ Thermal Evaporator. In the case of inverted architecture devices, ZnO was used as the bottom transparent electrode (replacing PEDOT:PSS), where the ZnO solution was prepared in a nitrogen glovebox by mixing tetrahydrofuran and diethylzinc (2:1). The fresh ZnO solution was then spin-coated atop the clean ITO substrates at 4000 rpm for 30 seconds and then placed on a hotplate at 110 °C for 15 minutes. Following active layer spin-coating, the inverted devices were pumped down under vacuum ($<10^{-7}$ torr), and 7 nm of MoO_x and 100 nm thick Ag electrode were deposited on top of the active layer by thermal evaporation. The electrode overlap area was 0.22 cm^2 for both conventional and inverted devices. The active area of the device was determined using an optical microscope.

OSC Device Testing: Photovoltaic characteristic measurements were carried out inside a N_2 filled glove box. Solar-cell device properties were measured under illumination by a simulated 100 mW cm^{-2} AM1.5 G light source using a 300 W Xe arc lamp with an AM 1.5 global filter. The irradiance was adjusted to 1 Sun with a standard silicon photovoltaic cell calibrated by the National Renewable Energy Laboratory. No spectral mismatch correction was applied. A Keithley 2635A source measurement unit was used to scan the voltage applied to the solar cell between -2 to 1 V at a speed of 0.43 V/s with a dwell time of 46 ms. Scans were performed in both the forward and reverse directions, with no unusual behavior observed. Between eight and 30 individual solar cell devices were tested for each blend reported. The error associated with the reported PCE values is ±0.2%. External quantum efficiency (EQE) for the OSCs was measured using a 75 W Xe light source, monochromator, optical chopper (138 Hz), and a lock-in amplifier. Power-density calibration of the EQE characteristics was achieved using a calibrated silicon photodiode from Newport.

Photoluminescence Quantum Efficiency Measurements: The PLQE was determined using method previously described by De Mello et al..[97] Samples were placed in an integrating sphere and photoexcited using a 658 nm continuous-wave laser. The laser and emission signals were measured and quantified using calibrated Andor iDus DU420A BVF Si and Andor CCD-1430 InGaAs detectors.

TA Spectroscopy: TA was performed on a setup powered using a commercially available Ti:sapphire amplifier (Spectra Physics Solstice Ace). The amplifier operates at 1 kHz and generates 100 fs pulses centered at 800 nm with an output of 7 W. A TOPAS optical parametric amplifier (OPA) was used to provide the tunable $\approx$100 fs pump pulses. The probe was provided by a broadband IR noncollinear optical parametric amplifier (NOPA). The probe pulses are collected with an InGaAs dual-line array detector (Hamamatsu G11608-512DA), driven and read out by a custom-built board from Stresing Entwicklungsbüro. The probe beam was split into two identical beams by a 50/50 beamsplitter. This allowed for the use of a second reference beam which also passes through the sample but does not interact with the pump. The role of the reference was to correct for any shot-to-shot fluctuations in the probe that would otherwise greatly increase the structured noise in our experiments. Through this arrangement, very small signals with a $\frac{\Delta T}{T} = 1 \times 10^{-5}$ could be measured.

trEPR Spectroscopy: EPR samples were fabricated by spin-coating solutions under identical conditions to the optimized devices onto Mylar substrates, which were subsequently cut into strips with a width of 3 mm. To ensure the flexible Mylar substrates did not bend during the spin coating process, they were mounted onto rigid glass substrates using adhesive tape. The strips were placed in quartz EPR tubes which

were sealed in a nitrogen glovebox with a bi-component resin (Devcon 5-Minute Epoxy), ensuring that all EPR measurements were performed without oxygen exposure.

All trEPR spectra were recorded on a Bruker Elexsys E580 X-band spectrometer, equipped with a nitrogen gas-flow cryostat for sample temperature control. The sample temperature was maintained with an Oxford Instruments CF935O cryostat and controlled with an Oxford Instruments ITC503. Laser pulses for trEPR were collimated into the cryostat and resonator windows from a multi-mode optical fiber, ThorLabs FT600UMT. Sample excitation at 532 nm with an energy of 2 mJ per pulse and a duration of 7 ns was provided by the residual 2nd harmonic output of a Newport/Spectra Physics Lab 170 Quanta Ray Nd:YAG pulsed laser, operating at 20 Hz. The trEPR signal was recorded through a Bruker SpecJet II transient recorder with timing synchronization by a Stanford Research Systems DG645 delay generator. The instrument response time was about 200 ns. The spectra were acquired with 2 mW microwave power and averaging 400 transient signals at each field position.

From the datasets obtained, the transient EPR spectra at different time delays after the laser pulse have been extracted and averaged over a time window of 0.5 μs. Spectral simulations have been performed using the core functions pepper and esfit of the open-source MATLAB toolbox EasySpin.[94] The parameters included in our best-fit simulations are the ZFS parameters (D and E), the triplet population sublevels (p_1, p_2, p_3) and the line broadening (assumed as only Lorentzian to not over-parametrize the fitting). For the calculation of spin polarization, the populations of the spin-triplet sublevels at zero field were calculated (T_x, T_y, T_z) in the fitting program and used by EasySpin to simulate the trEPR spectrum at resonant fields. For all the simulations, the g tensor was assumed isotropic with $g_{iso} = 2.002$. To carry out our least-square fittings, a user-defined simulation function has been developed which allows the fitting of parameters, such as the spin populations of the triplet sublevels. All the fits were carried out using a Nelder/Mead downhill simplex optimization algorithm.

PLDMR Spectroscopy: PLDMR samples were prepared in the same way as the trEPR samples, whereby the EPR tubes were sealed under inert helium atmosphere to measure at cryogenic (10 K) temperatures. PLDMR measurements were carried out in a modified X-band spectrometer (Bruker E300) equipped with a continuous-flow helium cryostat (Oxford ESR 900) and a microwave cavity (Bruker ER4104OR, 9.43 GHz) with optical access. Optical irradiation was performed with a 473 nm continuous wave laser (Cobolt) from one side opening of the cavity. PL was detected with a silicon photodiode (Hamamatsu Si photodiode S2281) on the opposite opening of the cavity, using a 561 nm longpass filter to reject the excitation wavelength. The PL signal was amplified by a current/voltage amplifier (Femto DHPCA-100) and recorded by lock-in detector (Ametek SR 7230), referenced by TTL-modulating the microwaves with 517 Hz. Microwaves were generated with a microwave signal generator (Anritsu MG3694C), amplified to 3W (Microsemi), and guided into the cavity.

Supporting Information

Supporting Information is available from the Wiley Online Library or from the author.

Acknowledgements

Conflict of Interest

The authors declare no conflict of interest.

Data Availability Statement

The data that support the findings of this study are available from the corresponding author upon reasonable request.

Keywords

[1] Q. Liu, Y. Jiang, K. Jin, J. Qin, J. Xu, W. Li, J. Xiong, J. Liu, Z. Xiao, K. Sun, S. Yang, X. Zhang, L. Ding, *Sci. Bull.* **2020**, *65*, 272.

[2] P. Bi, S. Zhang, Z. Chen, Y. Xu, Y. Cui, T. Zhang, J. Ren, J. Qin, L. Hong, X. Hao, J. Hou, *Joule* **2021**, *5*, 2408.

[3] Y. Cai, Y. Li, R. Wang, H. Wu, Z. Chen, J. Zhang, Z. Ma, X. Hao, Y. Zhao, C. Zhang, F. Huang, Y. Sun, *Adv. Mater.* **2021**, *33*, 2101733.

[4] Y. Cui, Y. Xu, H. Yao, P. Bi, L. Hong, J. Zhang, Y. Zu, T. Zhang, J. Qin, J. Ren, Z. Chen, C. He, X. Hao, Z. Wei, J. Hou, *Adv. Mater.* **2021**, *33*, 2102420.

[5] S. Bao, H. Yang, H. Fan, J. Zhang, Z. Wei, C. Cui, Y. Li, *Adv. Mater.* **2021**, *33*, 2105301.

[6] S. M. Menke, N. A. Ran, G. C. Bazan, R. H. Friend, *Joule* **2018**, *2*, 25.

[7] X.-K. Chen, D. Qian, Y. Wang, T. Kirchartz, W. Tress, H. Yao, J. Yuan, M. Hülsbeck, M. Zhang, Y. Zou, Y. Sun, Y. Li, J. Hou, O. Inganäs, V. Coropceanu, J.-L. Bredas, F. Gao, *Nat. Energy* **2021**, *6*, 799.

[8] S. Liu, J. Yuan, W. Deng, M. Luo, Y. Xie, Q. Liang, Y. Zou, Z. He, H. Wu, Y. Cao, *Nat. Photonics* **2020**, *14*, 300.

[9] J. Benduhn, K. Tvingstedt, F. Piersimoni, S. Ullbrich, Y. Fan, M. Tropiano, K. A. McGarry, O. Zeika, M. K. Riede, C. J. Douglas, S. Barlow, S. R. Marder, D. Neher, D. Spoltore, K. Vandewal, *Nat. Energy* **2017**, *2*, 17053.

[10] W. Shockley, H. J. Queisser, *J. Appl. Phys.* **1961**, *32*, 510.

[11] R. T. Ross, *J. Chem. Phys.* **1967**, *46*, 4590.

[12] U. Rau, *Phys. Rev. B* **2007**, *76*, 085303.

[13] B. Geffroy, P. le Roy, C. Prat, *Polym. Int.* **2006**, *55*, 572.

[14] D. Qian, Z. Zheng, H. Yao, W. Tress, T. R. Hopper, S. Chen, S. Li, J. Liu, S. Chen, J. Zhang, X.-K. Liu, B. Gao, L. Ouyang, Y. Jin,

G. Pozina, I. A. Buyanova, W. M. Chen, O. Inganäs, V. Coropceanu, J.-L. Bredas, H. Yan, J. Hou, F. Zhang, A. A. Bakulin, F. Gao, *Nat. Mater.* **2018**, *17*, 703.

[15] A. Classen, C. L. Chochos, L. Lüer, V. G. Gregoriou, J. Wortmann, A. Osvet, K. Forberich, I. McCulloch, T. Heumüller, C. J. Brabec, *Nat. Energy* **2020**, *5*, 711.

[16] F. D. Eisner, M. Azzouzi, Z. Fei, X. Hou, T. D. Anthopoulos, T. J. S. Dennis, M. Heeney, J. Nelson, *J. Am. Chem. Soc.* **2019**, *141*, 6362.

[17] J. Hou, O. Inganäs, R. H. Friend, F. Gao, *Nat. Mater.* **2018**, *17*, 119.

[18] R. Englman, J. Jortner, *Mol. Phys.* **1970**, *18*, 145.

[19] A. Zampetti, A. Minotto, F. Cacialli, *Adv. Funct. Mater.* **2019**, *29*, 1807623.

[20] A. J. Gillett, A. Privitera, R. Dilmurat, A. Karki, D. Qian, A. Pershin, G. Londi, W. K. Myers, J. Lee, J. Yuan, S.-J. Ko, M. K. Riede, F. Gao, G. C. Bazan, A. Rao, T.-Q. Nguyen, D. Beljonne, R. H. Friend, *Nature* **2021**, *597*, 666.

[21] R. Wang, J. Xu, L. Fu, C. Zhang, Q. Li, J. Yao, X. Li, C. Sun, Z.-G. Zhang, X. Wang, Y. Li, J. Ma, X. Miao, *J. Am. Chem. Soc.* **2021**, *143*, 4359.

[22] Z. Chen, X. Chen, Z. Jia, G. Zhou, J. Xu, Y. Wu, X. Xia, X. Li, X. Zhang, C. Deng, Y. Zhang, X. Lu, W. Liu, C. Zhang, Y. (Michael) Yang, H. Zhu, *Joule* **2021**, *5*, 1832.

[23] J. M. Marin-Beloqui, D. T. W. Toolan, N. A. Panjwani, S. Limbu, J. Kim, T. M. Clarke, *Adv. Energy Mater.* **2021**, *11*, 2100539.

[24] J. Yuan, Y. Zhang, L. Zhou, G. Zhang, H.-L. Yip, T.-K. Lau, X. Lu, C. Zhu, H. Peng, P. A. Johnson, M. Leclerc, J. Cao, J. Ulanski, Y. Li, Y. Zou, *Joule* **2019**, *3*, 1140.

[25] S. M. Menke, A. Sadhanala, M. Nikolka, N. A. Ran, M. K. Ravva, S. Abdel-Azeim, H. L. Stern, M. Wang, H. Sirringhaus, T.-Q. Nguyen, J.-L. Brédas, G. C. Bazan, R. H. Friend, *ACS Nano* **2016**, *10*, 10736.

[26] A. Rao, P. C. Y. Chow, S. Gélinas, C. W. Schlenker, C.-Z. Li, H.-L. Yip, A. K.-Y. Jen, D. S. Ginger, R. H. Friend, *Nature* **2013**, *500*, 435.

[27] I. Ramirez, A. Privitera, S. Karuthedath, A. Jungbluth, J. Benduhn, A. Sperlich, D. Spoltore, K. Vandewal, F. Laquai, M. Riede, *Nat. Commun.* **2021**, *12*, 471.

[28] E. M. Speller, A. J. Clarke, N. Aristidou, M. F. Wyatt, L. Francàs, G. Fish, H. Cha, H. K. H. Lee, J. Luke, A. Wadsworth, A. D. Evans, I. McCulloch, J.-S. Kim, S. A. Haque, J. R. Durrant, S. D. Dimitrov, W. C. Tsoi, Z. Li, *ACS Energy Lett.* **2019**, *4*, 846.

[29] E. M. Speller, J. D. McGettrick, B. Rice, A. M. Telford, H. K. H. Lee, C.-H. Tan, C. S. De Castro, M. L. Davies, T. M. Watson, J. Nelson, J. R. Durrant, Z. Li, W. C. Tsoi, *ACS Appl. Mater. Interfaces* **2017**, *9*, 22739.

[30] I. Sudakov, M. Van Landeghem, R. Lenaerts, W. Maes, S. Van Doorslaer, E. Goovaerts, *Adv. Energy Mater.* **2020**, *10*, 2002095.

[31] K. Vandewal, S. Mertens, J. Benduhn, Q. Liu, *J. Phys. Chem. Lett.* **2020**, *11*, 129.

[32] V. Coropceanu, X.-K. Chen, T. Wang, Z. Zheng, J.-L. Brédas, *Nat. Rev. Mater.* **2019**, *4*, 689.

[33] A. Karki, A. J. Gillett, R. H. Friend, T.-Q. Nguyen, *Adv. Energy Mater.* **2021**, *11*, 2003441.

[34] C. W. Schlenker, K.-S. Chen, H.-L. Yip, C.-Z. Li, L. R. Bradshaw, S. T. Ochsenbein, F. Ding, X. S. Li, D. R. Gamelin, A. K.-Y. Jen, D. S. Ginger, *J. Am. Chem. Soc.* **2012**, *134*, 19661.

[35] M. Liedtke, A. Sperlich, H. Kraus, A. Baumann, C. Deibel, M. J. M. Wirix, J. Loos, C. M. Cardona, V. Dyakonov, *J. Am. Chem. Soc.* **2011**, *133*, 9088.

[36] U. E. Steiner, T. Ulrich, *Chem. Rev.* **1989**, *89*, 51.

[37] A. J. Gillett, C. Tonnelé, G. Londi, G. Ricci, M. Catherin, D. M. L. Unson, D. Casanova, F. Castet, Y. Olivier, W. M. Chen, E. Zaborova, E. W. Evans, B. H. Drummond, P. J. Conaghan, L.-S. Cui, N. C. Greenham, Y. Puttisong, F. Fages, D. Beljonne, R. H. Friend, *Nat. Commun.* **2021**, *12*, 6640.

[38] J. Benduhn, F. Piersimoni, G. Londi, A. Kirch, J. Widmer, C. Koerner, D. Beljonne, D. Neher, D. Spoltore, K. Vandewal, *Adv. Energy Mater.* **2018**, *8*, 1800451.

[39] A. Köhler, D. Beljonne, *Adv. Funct. Mater.* **2004**, *14*, 11.

[40] M.-A. Pan, T.-K. Lau, Y. Tang, Y.-C. Wu, T. Liu, K. Li, M.-C. Chen, X. Lu, W. Ma, C. Zhan, *J. Mater. Chem. A* **2019**, *7*, 20713.

[41] M. Zhang, L. Zhu, G. Zhou, T. Hao, C. Qiu, Z. Zhao, Q. Hu, B. W. Larson, H. Zhu, Z. Ma, Z. Tang, W. Feng, Y. Zhang, T. P. Russell, F. Liu, *Nat. Commun.* **2021**, *12*, 309.

[42] A. A. Bakulin, S. D. Dimitrov, A. Rao, P. C. Y. Chow, C. B. Nielsen, B. C. Schroeder, I. McCulloch, H. J. Bakker, J. R. Durrant, R. H. Friend, *J. Phys. Chem. Lett.* **2013**, *4*, 209.

[43] F. Kraffert, R. Steyrleuthner, S. Albrecht, D. Neher, M. C. Scharber, R. Bittl, J. Behrends, *J. Phys. Chem. C* **2014**, *118*, 28482.

[44] M. S. Kotova, G. Londi, J. Junker, S. Dietz, A. Privitera, K. Tvingstedt, D. Beljonne, A. Sperlich, V. Dyakonov, *Mater. Horiz.* **2020**, *7*, 1641.

[45] V. Dyakonov, G. Rösler, M. Schwoerer, E. L. Frankevich, *Phys. Rev. B* **1997**, *56*, 3852.

[46] J. Lee, S.-J. Ko, M. Seifrid, H. Lee, C. McDowell, B. R. Luginbuhl, A. Karki, K. Cho, T.-Q. Nguyen, G. C. Bazan, *Adv. Energy Mater.* **2018**, *8*, 1801209.

[47] H. Yao, Y. Cui, R. Yu, B. Gao, H. Zhang, J. Hou, *Angew. Chem.* **2017**, *129*, 3091.

[48] C. Li, J. Zhou, J. Song, J. Xu, H. Zhang, X. Zhang, J. Guo, L. Zhu, D. Wei, G. Han, J. Min, Y. Zhang, Z. Xie, Y. Yi, H. Yan, F. Gao, F. Liu, Y. Sun, *Nat. Energy* **2021**, *6*, 605.

[49] S.-H. Liao, H.-J. Jhuo, Y.-S. Cheng, S.-A. Chen, *Adv. Mater.* **2013**, *25*, 4766.

[50] A. Karki, J. Vollbrecht, A. J. Gillett, P. Selter, J. Lee, Z. Peng, N. Schopp, A. L. Dixon, M. Schrock, V. Nádaždy, F. Schauer, H. Ade, B. F. Chmelka, G. C. Bazan, R. H. Friend, T. Nguyen, *Adv. Energy Mater.* **2020**, *10*, 2001203.

[51] S. Karuthedath, J. Gorenflot, Y. Firdaus, N. Chaturvedi, C. S. P. De Castro, G. T. Harrison, J. I. Khan, A. Markina, A. H. Balawi, T. A. Dela Peña, W. Liu, R.-Z. Liang, A. Sharma, S. H. K. Paleti, W. Zhang, Y. Lin, E. Alarousu, D. H. Anjum, P. M. Beaujuge, S. De Wolf, I. McCulloch, T. D. Anthopoulos, D. Baran, D. Andrienko, F. Laquai, *Nat. Mater.* **2021**, *20*, 378.

[52] L. Franco, A. Toffoletti, M. Ruzzi, L. Montanari, C. Carati, L. Bonoldi, R. Po, *J. Phys. Chem. C* **2013**, *117*, 1554.

[53] S. A. J. Thomson, J. Niklas, K. L. Mardis, C. Mallares, I. D. W. Samuel, O. G. Poluektov, *J. Phys. Chem. C* **2017**, *121*, 22707.

[54] A. Karki, J. Vollbrecht, A. J. Gillett, S. S. Xiao, Y. Yang, Z. Peng, N. Schopp, A. L. Dixon, S. Yoon, M. Schrock, H. Ade, G. N. M. Reddy, R. H. Friend, T.-Q. Nguyen, *Energy Environ. Sci.* **2020**, *13*, 3679.

[55] I. A. Howard, R. Mauer, M. Meister, F. Laquai, *J. Am. Chem. Soc.* **2010**, *132*, 14866.

[56] S. D. Dimitrov, S. Wheeler, D. Niedzialek, B. C. Schroeder, H. Utzat, J. M. Frost, J. Yao, A. Gillett, P. S. Tuladhar, I. McCulloch, J. Nelson, J. R. Durrant, *Nat. Commun.* **2015**, *6*, 6501.

[57] C. Keiderling, S. Dimitrov, J. R. Durrant, *J. Phys. Chem. C* **2017**, *121*, 14470.

[58] P. C. Y. Chow, S. Albert-Seifried, S. Gélinas, R. H. Friend, *Adv. Mater.* **2014**, *26*, 4851.

[59] Y. Tamai, Y. Fan, V. O. Kim, K. Ziabrev, A. Rao, S. Barlow, S. R. Marder, R. H. Friend, S. M. Menke, *ACS Nano* **2017**, *11*, 12473.

[60] S. Richert, C. E. Tait, C. R. Timmel, *J. Magn. Reson.* **2017**, *280*, 103.

[61] J. Niklas, S. Beaupré, M. Leclerc, T. Xu, L. Yu, A. Sperlich, V. Dyakonov, O. G. Poluektov, *J. Phys. Chem. B* **2015**, *119*, 7407.

[62] T. Biskup, *Front. Chem.* **2019**, *7*, 10.

[63] S. Weber, in *EMagRes*, John Wiley & Sons, Ltd, Chichester, UK, **2017**, pp. 255–270.

[64] C. Hintze, U. E. Steiner, M. Drescher, *ChemPhysChem* **2017**, *18*, 6.

[65] S. Gélinas, A. Rao, A. Kumar, S. L. Smith, A. W. Chin, J. Clark, T. S. van der Poll, G. C. Bazan, R. H. Friend, *Science* **2014**, *343*, 512.

[66] C. D. Buckley, D. A. Hunter, P. J. Hore, K. A. McLauchlan, *Chem. Phys. Lett.* **1987**, *135*, 307.

[67] J. Behrends, A. Sperlich, A. Schnegg, T. Biskup, C. Teutloff, K. Lips, V. Dyakonov, R. Bittl, *Phys. Rev. B* **2012**, *85*, 125206.

[68] A. E. Cohen, *J. Phys. Chem. A* **2009**, *113*, 11084.

[69] P. Kohn, Z. Rong, K. H. Scherer, A. Sepe, M. Sommer, P. Müller-Buschbaum, R. H. Friend, U. Steiner, S. Hüttner, *Macromolecules* **2013**, *46*, 4002.

[70] N. D. Treat, A. Varotto, C. J. Takacs, N. Batara, M. Al-Hashimi, M. J. Heeney, A. J. Heeger, F. Wudl, C. J. Hawker, M. L. Chabinyc, *J. Am. Chem. Soc.* **2012**, *134*, 15869.

[71] E. Buchaca-Domingo, A. J. Ferguson, F. C. Jamieson, T. McCarthy-Ward, S. Shoaee, J. R. Tumbleston, O. G. Reid, L. Yu, M.-B. Madec, M. Pfannmöller, F. Hermerschmidt, R. R. Schröder, S. E. Watkins, N. Kopidakis, G. Portale, A. Amassian, M. Heeney, H. Ade, G. Rumbles, J. R. Durrant, N. Stingelin, *Mater. Horiz.* **2014**, *1*, 270.

[72] B. A. Collins, Z. Li, J. R. Tumbleston, E. Gann, C. R. Mcneill, H. Ade, *Adv. Energy Mater.* **2013**, *3*, 65.

[73] N. C. Cates, R. Gysel, Z. Beiley, C. E. Miller, M. F. Toney, M. Heeney, I. McCulloch, M. D. McGehee, *Nano Lett.* **2009**, *9*, 4153.

[74] W. Chen, T. Xu, F. He, W. Wang, C. Wang, J. Strzalka, Y. Liu, J. Wen, D. J. Miller, J. Chen, K. Hong, L. Yu, S. B. Darling, *Nano Lett.* **2011**, *11*, 3707.

[75] P. Westacott, J. R. Tumbleston, S. Shoaee, S. Fearn, J. H. Bannock, J. B. Gilchrist, S. Heutz, J. DeMello, M. Heeney, H. Ade, J. Durrant, D. S. McPhail, N. Stingelin, *Energy Environ. Sci.* **2013**, *6*, 2756.

[76] H. Utzat, S. D. Dimitrov, S. Wheeler, E. Collado-Fregoso, P. S. Tuladhar, B. C. Schroeder, I. McCulloch, J. R. Durrant, *J. Phys. Chem. C* **2017**, *121*, 9790.

[77] F. C. Jamieson, E. B. Domingo, T. McCarthy-Ward, M. Heeney, N. Stingelin, J. R. Durrant, *Chem. Sci.* **2012**, *3*, 485.

[78] D. W. Gehrig, I. A. Howard, S. Sweetnam, T. M. Burke, M. D. McGehee, F. Laquai, *Macromol. Rapid Commun.* **2015**, *36*, 1054.

[79] J. A. Bartelt, Z. M. Beiley, E. T. Hoke, W. R. Mateker, J. D. Douglas, B. A. Collins, J. R. Tumbleston, K. R. Graham, A. Amassian, H. Ade, J. M. J. Fréchet, M. F. Toney, M. D. McGehee, *Adv. Energy Mater.* **2013**, *3*, 364.

[80] E. Salvadori, N. Luke, J. Shaikh, A. Leventis, H. Bronstein, C. W. M. Kay, T. M. Clarke, *J. Mater. Chem. A* **2017**, *5*, 24335.

[81] A. Karki, J. Vollbrecht, A. L. Dixon, N. Schopp, M. Schrock, G. N. M. Reddy, T.-Q. Nguyen, *Adv. Mater.* **2019**, *31*, 1903868.

[82] G. Zhou, H. Ding, L. Zhu, C. Qiu, M. Zhang, T. Hao, W. Feng, Y. Zhang, H. Zhu, F. Liu, *J. Energy Chem.* **2020**, *47*, 180.

[83] X. Shi, L. Zuo, S. B. Jo, K. Gao, F. Lin, F. Liu, A. K. Y. Jen, *Chem. Mater.* **2017**, *29*, 8369.

[84] L. Ye, H. Hu, M. Ghasemi, T. Wang, B. A. Collins, J.-H. Kim, K. Jiang, J. H. Carpenter, H. Li, Z. Li, T. McAfee, J. Zhao, X. Chen, J. L. Y. Lai, T. Ma, J.-L. Bredas, H. Yan, H. Ade, *Nat. Mater.* **2018**, *17*, 253.

[85] D. Di Nuzzo, A. Aguirre, M. Shahid, V. S. Gevaerts, S. C. J. Meskers, R. A. J. Janssen, *Adv. Mater.* **2010**, *22*, 4321.

[86] D. Carbonera, *Photosynth. Res.* **2009**, *102*, 403.

[87] J. Grüne, V. Dyakonov, A. Sperlich, *Mater. Horiz.* **2021**, *8*, 2569.

[88] P. A. Lane, X. Wei, Z. V. Vardeny, J. Partee, J. Shinar, *Phys. Rev. B* **1996**, *53*, R7580.

[89] S. S. Eaton, K. M. More, B. M. Sawant, G. R. Eaton, *J. Am. Chem. Soc.* **1983**, *105*, 6560.

[90] O. G. Poluektov, S. Filippone, N. Martín, A. Sperlich, C. Deibel, V. Dyakonov, *J. Phys. Chem. B* **2010**, *114*, 14426.

[91] O. G. Poluektov, J. Niklas, K. L. Mardis, S. Beaupré, M. Leclerc, C. Villegas, S. Erten-Ela, J. L. Delgado, N. Martín, A. Sperlich, V. Dyakonov, *Adv. Energy Mater.* **2014**, *4*, 1301517.

[92] C. A. Reed, R. D. Bolskar, *Chem. Rev.* **2000**, *100*, 1075.

[93] T. Biskup, M. Sommer, S. Rein, D. L. Meyer, M. Kohlstädt, U. Würfel, S. Weber, *Angew. Chem., Int. Ed.* **2015**, *54*, 7707.

[94] S. Stoll, A. Schweiger, *J. Magn. Reson.* **2006**, *178*, 42.

[95] J. Niklas, K. L. Mardis, B. P. Banks, G. M. Grooms, A. Sperlich, V. Dyakonov, S. Beaupré, M. Leclerc, T. Xu, L. Yu, O. G. Poluektov, *Phys. Chem. Chem. Phys.* **2013**, *15*, 9562.

[96] Y. Firdaus, V. M. Le Corre, S. Karuthedath, W. Liu, A. Markina, W. Huang, S. Chattopadhyay, M. M. Nahid, M. I. Nugraha, Y. Lin, A. Seitkhan, A. Basu, W. Zhang, I. McCulloch, H. Ade, J. Labram, F. Laquai, D. Andrienko, L. J. A. Koster, T. D. Anthopoulos, *Nat. Commun.* **2020**, *11*, 5220.

[97] J. C. de Mello, H. F. Wittmann, R. H. Friend, *Adv. Mater.* **1997**, *9*, 230.